

Recent progress on the LS-STAG immersed boundary method for complex fluids : Flow of shear-thinning liquids between eccentric rotating cylinders

O. Botella^{*,**}, M. Ait-Messaoud^{*,**}, A. Pertat^{*,**}, C. Rigal^{*,**} and Y. Cheny^{*,**}
Corresponding author: olivier.botella@univ-lorraine.fr

^{*}Université de Lorraine, LEMTA, UMR 7563, Vandoeuvre-lès-Nancy, F-54500, France.

^{**}CNRS, LEMTA, UMR 7563, Vandoeuvre-lès-Nancy, F-54500, France.

Abstract: This communication presents a progress report on flow computations of complex fluids performed with a well established Immersed Boundary (IB) method, the LS-STAG method (Cheny & Botella, Journal of Computational Physics 2010). The term “complex fluid” refers here to a material which has a viscoelastic or non-Newtonian behaviour, or both. One of the distinguished features of our IB method is to use level-set (LS) techniques in the cut-cells near the irregular boundary, where accurate discretization is of paramount importance for stability and accuracy of the computations. For this purpose, we have achieved an unified framework for the computation of the Navier-Stokes equations, viscoelastic constitutive law and non-Newtonian viscosity on the LS-STAG mesh. The method is validated for the flow of shear-thinning fluids between eccentric rotating cylinders for which experimental and computational data are available.

Keywords: Immersed boundary method, cut-cell method, Incompressible flows, non-Newtonian fluids, eccentric Taylor-Couette flow.

1 Introduction

This communication presents a progress report on an ongoing project aiming at the computation of complex fluid flows with a realistic constitutive law, which would take into account the pseudoplastic, viscoelastic and thixotropic behavior of the materials. The flow solver is based on the LS-STAG method, which is an immersed boundary (IB) method that allows the computation of flows in irregular or moving geometries on fixed Cartesian meshes, reducing thus the bookkeeping of body-fitted methods. The discretization in the cut-cells (i.e., the computational cells which are cut by the irregular boundary) is achieved by requiring that the global conservation properties of the Navier-Stokes equations are satisfied at the discrete level, resulting in a stable and accurate method and, thanks to the level-set representation of the IB boundary, at low computational costs. The LS-STAG method has been validated in [1, 2] for canonical Newtonian flows in both fixed and moving geometries.

In a recent work [3, 4] we have applied the LS-STAG method to viscoelastic flows, for which accurate discretization of the viscous stresses up to the cut-cells is of paramount importance for stability and accuracy. For this purpose, the LS-STAG discretization of the Newtonian stresses has been extended to the transport equation of the elastic stresses, such that the node-to-node oscillations of the stress variables are prevented by using a velocity-pressure-stress ($\mathbf{v} - p - \boldsymbol{\tau}$) staggered arrangement. The discretization of the Oldroyd-B constitutive equation is performed by constructing special quadratures which yield a globally conservative discretization up to the cut-cells. Results on popular benchmarks for viscoelastic flows shows that our IB method demonstrates an accuracy and robustness comparable to body-fitted methods up to large levels of elasticity.

The next step is to incorporate the pseudoplastic behavior in the numerical model. The crucial part for taking into account shear-thinning effects is the computation of the shear rate in the vicinity of the immersed

$\Gamma^{\text{ib}} = \partial\Omega^{\text{ib}}$ is implicitly represented by its signed distance function $\phi(x, y)$ (or level-set function, see *e.g.* [7] and references therein), which is discretized at the vertices of the rectangular cells. The level-set function is an efficient tool for computing all relevant geometry parameters of the cut-cells (such as their volume, projected areas, boundary conditions, ...), reducing thus the bookkeeping associated to the handling of complex geometries. Relevant geometry parameters for fluid cell $\Omega_{i,j}$ are its grid-size $\Delta x_i = x_i - x_{i-1}$, $\Delta y_j = y_j - y_{j-1}$, its volume $V_{i,j}$ (constructed in Ref. [2] from the values of $\phi_{i,j}$) and the ‘‘cell-face fraction’’ $\theta_{i,j}^u \in [0, 1]$ which represents the fluid fraction of the face of a cut-cell. For example, the fluid fraction of the east face of $\Omega_{i,j}$ in Fig. 1 is defined by linear interpolation of the level-set as :

$$\theta_{i,j}^u \equiv \frac{y_{i,j}^{\text{ib}} - y_{j-1}}{\Delta y_j} = \frac{\phi_{i,j-1}}{\phi_{i,j-1} - \phi_{i,j}} \quad \text{since } \phi(x_i, y_{i,j}^{\text{ib}}) = 0. \quad (2)$$

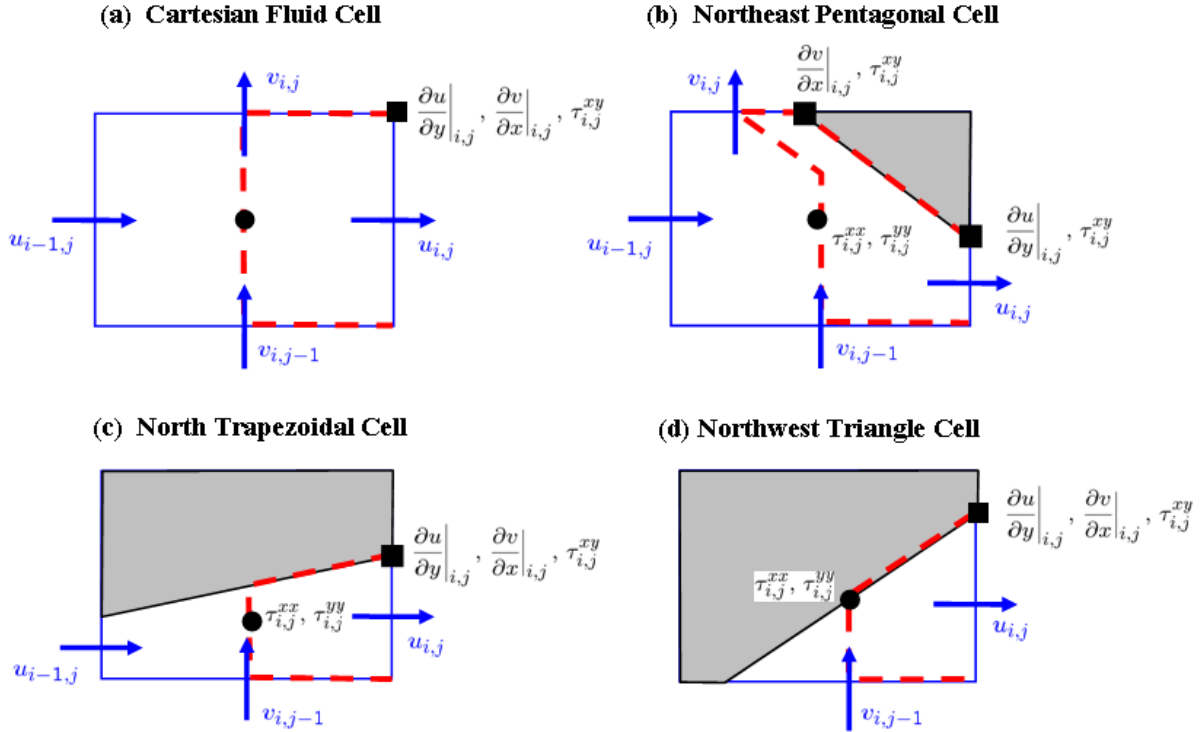


Figure 2: Sketch of the 4 generic fluid cells $\Omega_{i,j}$ and location of the normal and shear stresses.

Fig. 2 shows the 4 types of fluid cells which are present in the LS-STAG mesh : a Cartesian fluid cell away from the IB boundary, and 3 generic types of cut-cells (pentagon, trapezoidal and triangle). For each type of cells, the figure displays the half control volumes (CVs) that forms the $\Omega_{i,j}^u$ CV for discretizing the momentum equation (1a). For building the LS-STAG method in Refs. [2], we have enforced the strict conservation of total mass $\int_{\Omega_f} \nabla \cdot \mathbf{v} dV$, total momentum $\mathbf{P}(t) = \rho \int_{\Omega_f} \mathbf{v} dV$ and total kinetic energy $E_c(t) = \frac{1}{2} \int_{\Omega_f} |\mathbf{v}|^2 dV$ (when viscosity η becomes negligible) in each of the half CVs independently, such that any combination of half CVs yields a consistent discretization with the aforementioned global conservation properties. This results to a discrete pressure gradient which is dual to the divergence matrix, a skew-symmetric operator for the convective terms, and a viscous matrix which is positive definite. In the limiting case of meshes with Cartesian cells only (Fig. 2 (a)), the LS-STAG method recovers the case of the well-known MAC discretization for uniform grids and the method of Verstappen & Veldman [8] for non-uniform grids. The LS-STAG method has been validated in [1, 2] for canonical Newtonian flows in both fixed and moving geometries.

2.2 The LS-STAG method for viscoelastic flows

In Refs. [3, 4] the LS-STAG method has been extended to handle viscoelastic flows where the shear stress τ in Eq. (1a) is decomposed as : $\tau = \eta_s \mathbf{D} + \tau_e$, where η_s is the solvent viscosity (supposed constant) and τ_e is the viscoelastic tensor :

$$\tau_e = \begin{pmatrix} \tau_e^{xx} & \tau_e^{xy} \\ \tau_e^{xy} & \tau_e^{yy} \end{pmatrix}. \quad (3)$$

The viscoelastic tensor is governed by the Oldroyd-B constitutive equation [9], which is a hyperbolic transport equation.

A necessary step for extending the LS-STAG method to viscoelastic flows is the discretization of the constitutive equation in the cut-cells, such that the node-to-node oscillations of the stress variables are prevented. In [3, 4] we have achieved a fully staggered velocity-pressure-stress discretization of the Oldroyd-B equations such that the Cartesian staggered arrangement of Darwish & Whiteman [10] is recovered away from the IB boundary. In a Cartesian fluid cell (Fig. 2(a)), the viscoelastic stresses are located at the discretization points of the Newtonian stresses : *i.e.* the normal viscoelastic stresses $\tau_{i,j}^{xx}$ and $\tau_{i,j}^{yy}$ are at the center of the cell $\Omega_{i,j}$ and the viscoelastic shear stress $\tau_{i,j}^{xy}$ at its upper right corner. The generalization of this staggering to the cut-cells leads to the positioning shown in Fig. 2(b)-(d). Note that for the case of pentagonal cells (Fig. 2(b)), where the Newtonian shear stresses $\partial u/\partial y|_{i,j}$ and $\partial v/\partial x|_{i,j}$ are calculated at different vertices of the immersed boundary, we consider that $\tau_{i,j}^{xy}$ takes the same value at both vertices. In the context of a finite-volume method, this staggered arrangement introduces a different control volume for the constitutive equation of normal and shear stresses, which led us to develop special quadratures and interpolations that yield a globally conservative discretization up to the cut-cells. These interpolation rules are defined in [4] and will be employed in the next section devoted to the computation of non-Newtonian flows.

2.3 Extension of the LS-STAG method to non-Newtonian fluids

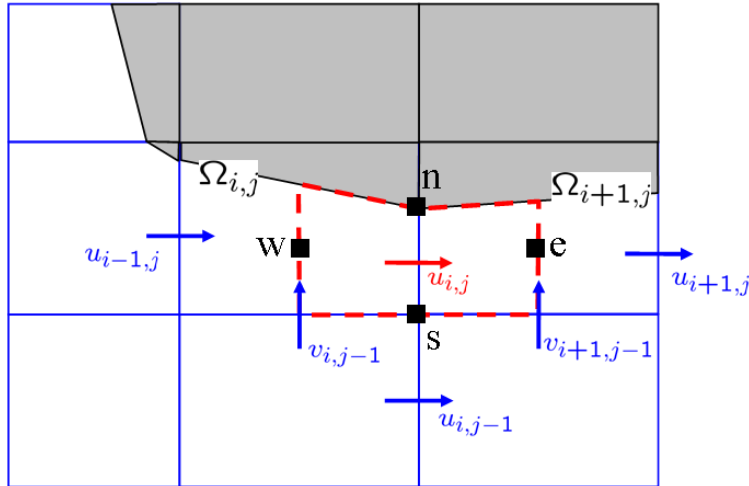


Figure 3: Relevant notations used for the discretization of non-Newtonian flow equations near the IB boundary. The shear rate is discretized at the center of the faces of $\Omega_{i,j}^u$, denoted with compass notations.

We consider now the application of the LS-STAG method to the case of non-Newtonian fluids, where the stress tensor takes the form :

$$\tau = \eta(\dot{\gamma}) \mathbf{D}, \quad (4)$$

and the shear rate $\dot{\gamma}$ is related to the second invariant of the rate-of-strain tensor \mathbf{D} :

$$\dot{\gamma} = \sqrt{\frac{1}{2} \mathbf{D} : \mathbf{D}} = \sqrt{2 \left[\frac{\partial u}{\partial x} \right]^2 + \left[\frac{\partial u}{\partial y} + \frac{\partial v}{\partial x} \right]^2 + 2 \left[\frac{\partial v}{\partial y} \right]^2}. \quad (5)$$

In the following, we will consider 2 popular models for non-Newtonian viscosity which have similar mathematical form [9]. The simplest is the Ostwald de Waele (or power-law) model :

$$\eta(\dot{\gamma}) = k \dot{\gamma}^{n-1}, \quad (6)$$

where k and n are 2 empirical curve-fitting parameters, known as the consistency and power-law index respectively. The consistency index k is a measure of the average viscosity of the fluid, and the power-law index n is a measure of the deviation of the fluid from Newtonian behaviour : the case $n = 1$ correspond to Newtonian fluid, for $n < 1$ the fluid is shear-thinning (or pseudoplastic), and for $n > 1$ the fluid is shear-thickening. The power-law model is widely used in engineering applications and has the property to give analytical solutions of the Navier-Stokes equations for canonical flows [9]. Its main shortcoming is the inability to predict the Newtonian plateaux that reaches the viscosity at low (where $\eta = \eta_0$) and high (where $\eta = \eta_\infty$) shear rate. These shortcomings are overcome by the Cross model :

$$\eta(\dot{\gamma}) = \eta_\infty + \frac{(\eta_0 - \eta_\infty)}{1 + (K \dot{\gamma})^m}, \quad (7)$$

where K and m are 2 fitting parameters. The Cross parameters can be related to the power-law parameters (6) by observing that $k = \eta_0 K^{-m}$ and $n = 1 - m$ in the limiting case where $\eta_0 \gg \eta_\infty$, $K \dot{\gamma} \gg 1$ and η_∞ small.

For the purpose of time-advancing the Navier-Stokes equations with an implicit-explicit fractional step method, the diffusive flux $\mathbf{F}^d = (F_u^d, F_v^d) = \int_\Omega \nabla \cdot \boldsymbol{\tau} \, dV$ of Eq. (1a) is split in an ‘‘implicit’’ and ‘‘explicit part’’, such as its components in the x -direction read :

$$F_u^d = F_u^{d,\text{impl}} + F_u^{d,\text{expl}}, \quad (8a)$$

with

$$F_u^{d,\text{impl}} = \int_\Gamma \eta(\dot{\gamma}) \left[\frac{\partial u}{\partial x} \vec{e}_x + \frac{\partial u}{\partial y} \vec{e}_y \right] \cdot d\vec{S}, \quad (8b)$$

$$F_u^{d,\text{expl}} = \int_\Gamma \eta(\dot{\gamma}) \left[\frac{\partial u}{\partial x} \vec{e}_x + \frac{\partial v}{\partial x} \vec{e}_y \right] \cdot d\vec{S}. \quad (8c)$$

where Γ represents the faces of a CV. With such a decomposition, the computation of the provisional velocities u and v in a fractional-step scheme can be totally decoupled. The discretization of these diffusive fluxes follows the lines of the discretization introduced in Ref. [2] for the Newtonian case, with the added difficulty that we also have to discretize the shear rate and the explicit fluxes. The methodology is best described in the case of the CV for $u_{i,j}$ represented in Fig 3. In this CV, the implicit flux (8b) is discretized as :

$$F_u^{d,\text{impl}} \cong \left[\eta(\dot{\gamma}|_e) \frac{\partial u}{\partial x} \Big|_{i,j} - \eta(\dot{\gamma}|_w) \frac{\partial u}{\partial x} \Big|_{i-1,j} \right] \theta_{i,j}^u \Delta y_j + \eta(\dot{\gamma}|_n) \frac{\partial u}{\partial y} \Big|_{i,j} \Delta x^{\text{ib},n} - \eta(\dot{\gamma}|_s) \frac{\partial u}{\partial y} \Big|_{i,j-1} \frac{1}{2} (\Delta x_i + \Delta x_{i+1}), \quad (9)$$

where we have used the notations of Fig. 2 for the normal and shear stresses. The finite difference-like quotient for the normal stress is [2] :

$$\frac{\partial u}{\partial x} \Big|_{i,j} \cong \frac{\theta_{i,j}^u u_{i,j} - \theta_{i-1,j}^u u_{i-1,j} + (\theta_{i-1,j}^u - \theta_{i,j}^u) u_{i,j}^{\text{ib}}}{V_{i,j} / \Delta y_j}. \quad (10)$$

This formula has been obtained thanks to the discretization of the incompressibility condition (1b) and the

requirement that the divergence theorem be verified on the LS-STAG mesh ; by construction (10) is valid for any computational cell and includes the non-homogeneous boundary condition $u_{i,j}^{\text{ib}}$ at the IB boundary. The discretization of the shear stress is similar to the Ghost Fluid method for elliptic equations [7], such as the quotient at location s of Fig. 3 is simply :

$$\frac{\partial u}{\partial y}\Big|_{i,j-1} \cong \frac{u_{i,j} - u_{i,j-1}}{\frac{1}{2}\theta_{i,j}^u \Delta y_j + \frac{1}{2}\theta_{i,j-1}^u \Delta y_{j-1}}, \quad (11a)$$

with $\theta_{i,j-1}^u = 1$ in the special case of Fig. 3, while at location n of the immersed boundary the following one-sided differential quotient is employed :

$$\frac{\partial u}{\partial y}\Big|_{i,j} \cong \frac{u(x_i, y_{i,j}^{\text{ib}}) - u_{i,j}}{\frac{1}{2}\theta_{i,j}^u \Delta y_j}. \quad (11b)$$

We now turn to the ‘‘explicit’’ flux (8c) which is discretized as :

$$F_u^{\text{d,expl}} \cong \left[\eta(\dot{\gamma}|_e) \frac{\partial u}{\partial x}\Big|_{i,j} - \eta(\dot{\gamma}|_w) \frac{\partial u}{\partial x}\Big|_{i-1,j} \right] \theta_{i,j}^u \Delta y_j + \eta(\dot{\gamma}|_n) \frac{\partial v}{\partial x}\Big|_n \Delta x^{\text{ib},n} - \eta(\dot{\gamma}|_s) \frac{\partial v}{\partial x}\Big|_{i,j-1} \frac{1}{2}(\Delta x_i + \Delta x_{i+1}). \quad (12)$$

Similar to the discretization of the ‘‘implicit’’ flux, the normal stresses are approximated by (10) and the shear stress at location s is analogous to (11a) :

$$\frac{\partial v}{\partial x}\Big|_{i,j-1} \cong \frac{v_{i+1,j-1} - v_{i,j-1}}{\frac{1}{2}\theta_{i,j-1}^u \Delta x_i + \frac{1}{2}\theta_{i+1,j-1}^u \Delta x_{i+1}}. \quad (13)$$

In contrast, the shear stress term $\partial v/\partial x|_n$ at the IB boundary was absent from the Newtonian discretization, and since the directional derivative is not normal to the immersed boundary there is no straightforward one-sided formula as in (11b). To approximate this term, we introduce a discretization of $\partial v/\partial x|_n$ which depends on the type of the cut-cells $\Omega_{i,j}$ and $\Omega_{i+1,j}$ of which n is a vertex. The discretization is summarized in the case of Fig. 2 where $\Omega_{i,j+1}$ is a trapezoidal cell and $\Omega_{i,j}$ is one of the 3 generic cut-cell of Fig. 3. In the case where $\Omega_{i,j}$ is a pentagonal cell (Fig. 2(a)), the discretization is :

$$\frac{\partial v}{\partial x}\Big|_n \cong \frac{\partial v}{\partial x}\Big|_{i,j} = \frac{v(x_{i,j}^{\text{ib}}, y_j) - v_{i,j}}{\frac{1}{2}\theta_{i,j}^v \Delta x_i}, \quad (14)$$

since the shear stress is assumed to have equal values at both IB vertices for pentagonal cut-cells. In the case where $\Omega_{i,j}$ is a trapezoidal cell (Fig. 2(b)), we simply assume that $\partial v/\partial x|_n = 0$ as it would be the case if the IB boundaries of $\Omega_{i,j}$ and $\Omega_{i+1,j}$ were horizontal. The same assumption $\partial v/\partial x|_n = 0$ is also made for the case of a triangular cell (Fig. 2(c)).

The discretization of the shear rate (5) uses the same differential quotients, but since the normal and shear stresses are located at different points, one needs to use the interpolation rules developed for the viscoelastic computations. For example, the shear rate at the immersed boundary location n of Fig. 3 is :

$$\dot{\gamma}|_n \cong \sqrt{2 \left[\overline{\frac{\partial u}{\partial x}}\Big|_{i,j} \right]^2 + \left[\frac{\partial u}{\partial y}\Big|_{i,j} + \frac{\partial v}{\partial x}\Big|_{i,j} \right]^2 + 2 \left[\overline{\frac{\partial v}{\partial y}}\Big|_{i,j} \right]^2}. \quad (15)$$

In this equation, the shear stresses are straightforwardly discretized by the procedure described above, but the normal stresses need to be interpolated by using the following volume-weighted interpolation rule denoted $(\overline{\cdot})$, which is defined in [4, 3] by :

$$\overline{\frac{\partial u}{\partial x}}\Big|_{i,j} = \left[\alpha_{i,j} V_{i,j} \frac{\partial u}{\partial x}\Big|_{i,j} + \alpha_{i+1,j} V_{i+1,j} \frac{\partial u}{\partial x}\Big|_{i+1,j} + \alpha_{i+1,j+1} V_{i+1,j+1} \frac{\partial u}{\partial x}\Big|_{i+1,j+1} + \alpha_{i,j+1} V_{i,j+1} \frac{\partial u}{\partial x}\Big|_{i,j+1} \right] / \tilde{V}_{i,j}, \quad (16)$$

where the volume $\tilde{V}_{i,j}$, which represents the area of the staggered CV for the elastic shear stresses, is constructed from the volume of the computational cells as :

$$\tilde{V}_{i,j} = \alpha_{i,j}V_{i,j} + \alpha_{i+1,j}V_{i+1,j} + \alpha_{i,j+1}V_{i,j+1} + \alpha_{i+1,j+1}V_{i+1,j+1}, \quad (17a)$$

and the coefficients $\alpha_{i,j}$ depend on the type of computational cells :

$$\alpha_{i,j} = \begin{cases} 0 & \text{if } \Omega_{i,j} \text{ is a solid cell,} \\ 1/3 & \text{if } \Omega_{i,j} \text{ is a triangular cell,} \\ 1/4 & \text{otherwise.} \end{cases} \quad (17b)$$

The time-advancement of the Navier-Stokes equations is based on an IMEX fractional-step method of first-order accuracy in time only, since we are only interested in steady solutions. The diffusive flux ($F_u^{d,impl}, F_v^{d,impl}$) is discretized with the backward Euler method, while the convective terms and diffusive flux ($F_u^{d,expl}, F_v^{d,expl}$) are treated with forward Euler. The shear rate at time t^{n+1} is extrapolated from its value at the previous time-step. This results in a fractional-step method where the computation of the provisional velocities \tilde{u}^{n+1} and \tilde{v}^{n+1} are fully decoupled. All steady solutions reported in the next section are obtained with a CFL number between 0.1 and 0.5, and we did not observe severe time-step restriction due to the explicit treatment of diffusive term ($F_u^{d,expl}, F_v^{d,expl}$).

3 Numerical simulation of non-Newtonian flows between eccentric cylinders

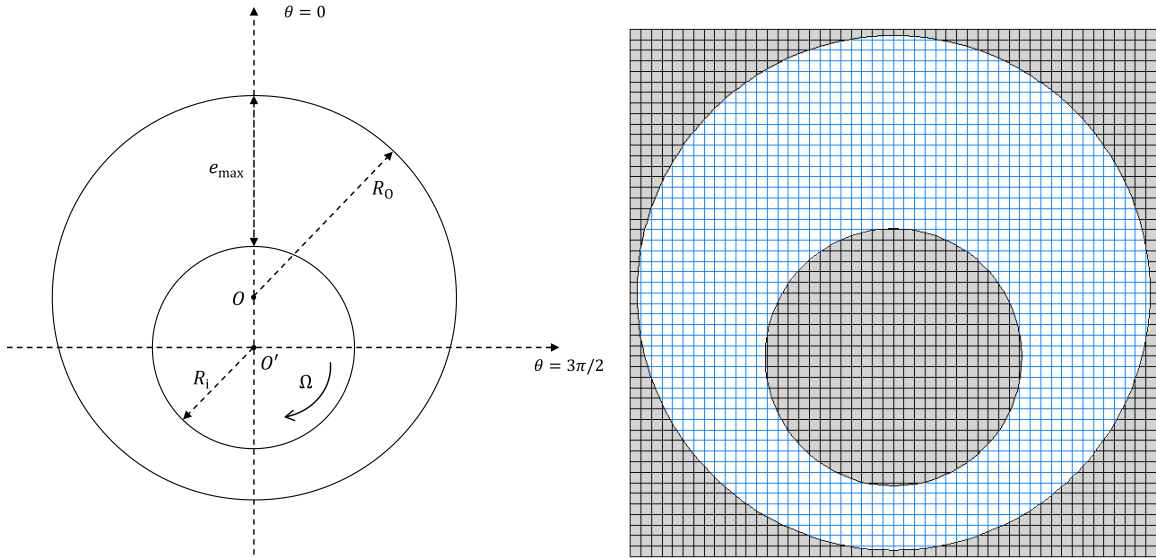


Figure 4: At left : Sketch of the geometry of the flow between eccentric cylinders ; the inner and outer cylinders have center at O' and O respectively, with radius $R_i = 20$ mm and $R_o = 40$ mm. At right : LS-STAG mesh of $N = 50$ cells in each direction.

The LS-STAG method is now validated for the flow of shear-thinning liquids between eccentric rotating cylinders. Since the early work of Reynolds (1886), this flow has been of significance in journal bearing lubrication theory. In Ref. [11], an analytic study has been performed for Newtonian fluids, in the case of creeping flows and low inertial effects. In particular, they have showed the appearance of a recirculation zone in the wide gap region when the eccentricity of the cylinders reached a critical value. These findings have been confirmed by various numerical studies (see Ref. [12] and references therein). For validating our methodology for non-Newtonian flows, we will use the database of Rigal [5] and Rigal *et al.* [6], who

%w/w	η_∞	η_0	K	m
0.10	0.00214	0.524	2.12	0.656
0.20	0.00273	2.26	4.55	0.701
0.30	0.00405	10.7	16.4	0.754
0.40	0.00458	30.1	44.2	0.765

Table 1: Parameters of the Cross model (7) for the fitting of the viscosity-shear rate curve of various aqueous xanthan solutions (% in weight).

have studied experimentally (PIV 2D) and numerically (FLUENT commercial software) the flow of xanthan solutions at various eccentricities. The flow domain (sketched in Fig. 4 left)) is the annular region between 2 eccentric cylinders of radius ratio $\bar{R} = R_i/R_o = 1/2$, where the inner cylinder is rotating in the clockwise sense with angular velocity Ω . The cylinders eccentricity is defined as $\delta = OO'/R_i$ and $e_{\max} = (1+\delta)R_i$ is the widest gap between the cylinders. The concentric case $\delta = 0$ corresponds to the well know Taylor-Couette flow. Various fluids have been considered : Emkarox (Newtonian with dynamic viscosity $\eta = 1.62 \text{ Pa} \cdot \text{s}$) and xanthan for various aqueous solutions (shear-thinning and viscoelastic). The shear-thinning behaviour of xanthan has been fitted with the Cross model (7), whose parameters are given in Table 1. For the angular velocities considered ($\Omega = 1 - 20 \text{ rad} \cdot \text{s}^{-1}$), the Taylor number is always below the critical values of $Ta_c = 33929$ and the flow is thus two-dimensional. The two-dimensionality of the flows has also been observed in the experiments. The level of elasticity of the xanthan flows has been evaluated as low (with Weissenberg number between 0.078 and 2.3) so that viscoelastic effects are neglected from the numerical modelling.

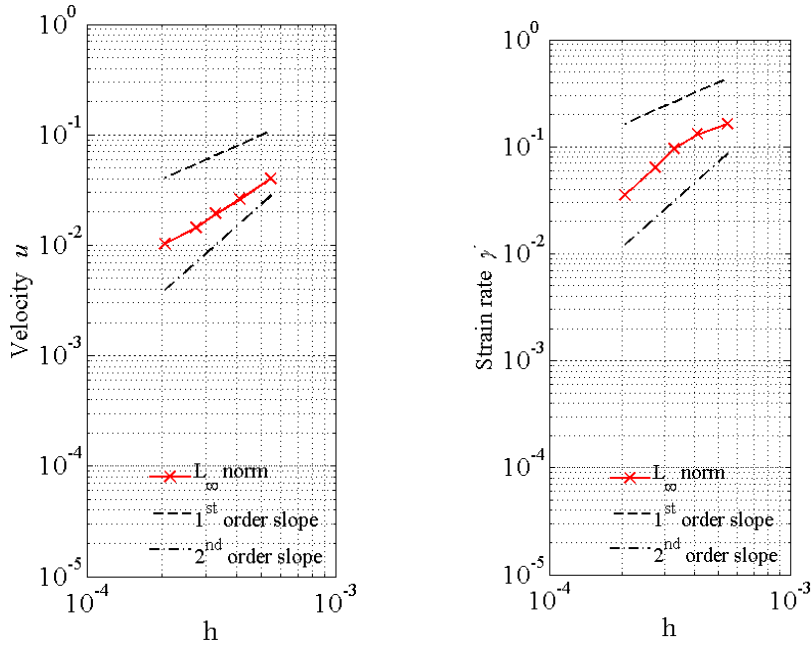


Figure 5: Normalized error in the maximum norm for the velocity u and the shear rate $\dot{\gamma}$ for the Taylor-Couette flow ($\delta = 0$) with $\Omega = 20 \text{ rad} \cdot \text{s}^{-1}$. The fluid is shear-thinning with power-law viscosity (6) with $k = 0.5647$ and $n = 0.389$. The meshes considered have $N = 150, 200, 250, 300$ and 400 cells in both directions.

For all the eccentricities δ we considered, the computational meshes consist in a square domain centered on the outer cylinder, with N uniform cells of size h in each direction (see Fig. 4 (right)). The steady state is considered reached when the normalized time-derivatives of the velocities are below the threshold $\epsilon = 10^{-8}$; with this tolerance we have checked that all flow features (velocity profiles, recirculation zone, forces and moments at IB boundaries) are fully converged. First the spatial accuracy of the LS-STAG method is assessed

by considering the concentric case $\delta = 0$. In this configuration, it is possible to obtain an analytical solution of the Navier-Stokes equations with the power-law model (6), which reads in polar coordinates as [13] :

$$v_r = 0, \quad v_\theta(r) = \frac{r^{-2/n} - R_o^{-2/n}}{R_i^{-2/n} - R_o^{-2/n}} r \Omega. \quad (18)$$

Fig. 5 shows the errors obtained on a series of meshes for the case of a power-law fitting of the viscosity curve of the xanthan 20%. In accordance with the accuracy tests performed in [2] for the Couette flow for Newtonian fluids, we obtain a superlinear convergence rate for u and $\dot{\gamma}$. This results shows that the computation of the non-Newtonian viscosity does not diminish the order of accuracy of the LS-STAG method.

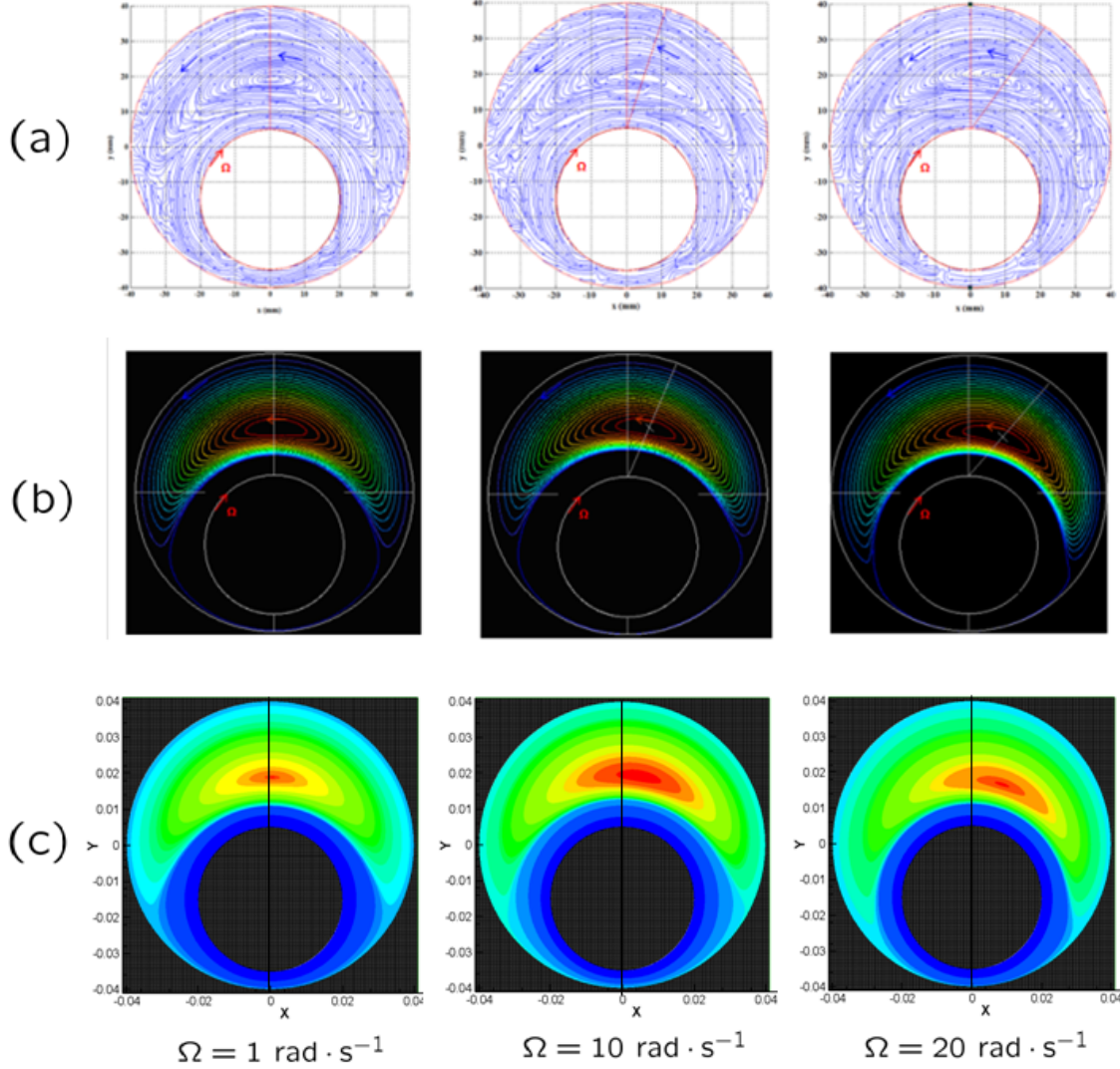


Figure 6: Streamlines for the flow of xanthan 0.10% at eccentricity $\delta = 0.75$ for various values of the inner cylinder angular velocity Ω : (a) PIV visualization of [6, 5] ; (b) FLUENT computations [6, 5]; (c) LS-STAG computations.

The LS-STAG code is now validated on non-coaxial configurations, where PIV results and FLUENT computations are available [6, 5]. All LS-STAG results reported have been obtained on a mesh with $N = 400$ cells in each directions, which gives about 88,000 fluid cells, corresponding to 57% of all computational cells. A grid refinement study with meshes of size $N = 100, 200, 400$ and 600 showed that the results obtained on the two finest mesh were indistinguishables. In comparison, the FLUENT results have been obtained on

a body conformal curvilinear mesh of 220,000 cells, more than twice as large as our $N = 400$ mesh. The flow is characterized by the appearance of a large secondary flow that appears in the widest gap region when the eccentricity reaches a critical value δ_c . For Newtonian fluids, all studies agree that the appearance of the recirculation zone is independent of the Reynolds number and is thus a purely geometrical phenomenon. For non-Newtonian fluids, Refs. [6, 5] observe that the appearance of the zone is delayed by shear-thinning effects. As an illustration, Fig. 6 compares the streamlines of the flow of xanthan 10% obtained by the experiments and the 2 numerical codes. All 3 studies shows a recirculation zone of comparable shape, size, and position. At low Reynolds number, the vortex zone is symmetric and centered on the line $\theta = 0$. As the cylinder rotation Ω is increased, the vortex zone becomes asymmetric and moves downstream due to the increase of the inertial effects. For the same flow configuration (xanthan 10%, $\delta = 0.75$), Fig. 7 compares the tangential velocity profiles for different cylinder rotation Ω along the axis $\theta = 0$ that goes through the secondary flow. We note that the results obtained by LS-STAG and FLUENT are in very good agreement. Discrepancies with the experiments appear in the vicinity of the rotating cylinder, where the PIV measurements are scattered, and most notably in the recirculation zone. In this region where the velocities are very weak, these discrepancies may be due to the tolerance of the measurements or the fact that the numerical solutions do not take into account the viscoelastic properties of the flow. Nonetheless, all three methods capture the monotonic decrease of the intensity of the vortex as Ω increases.

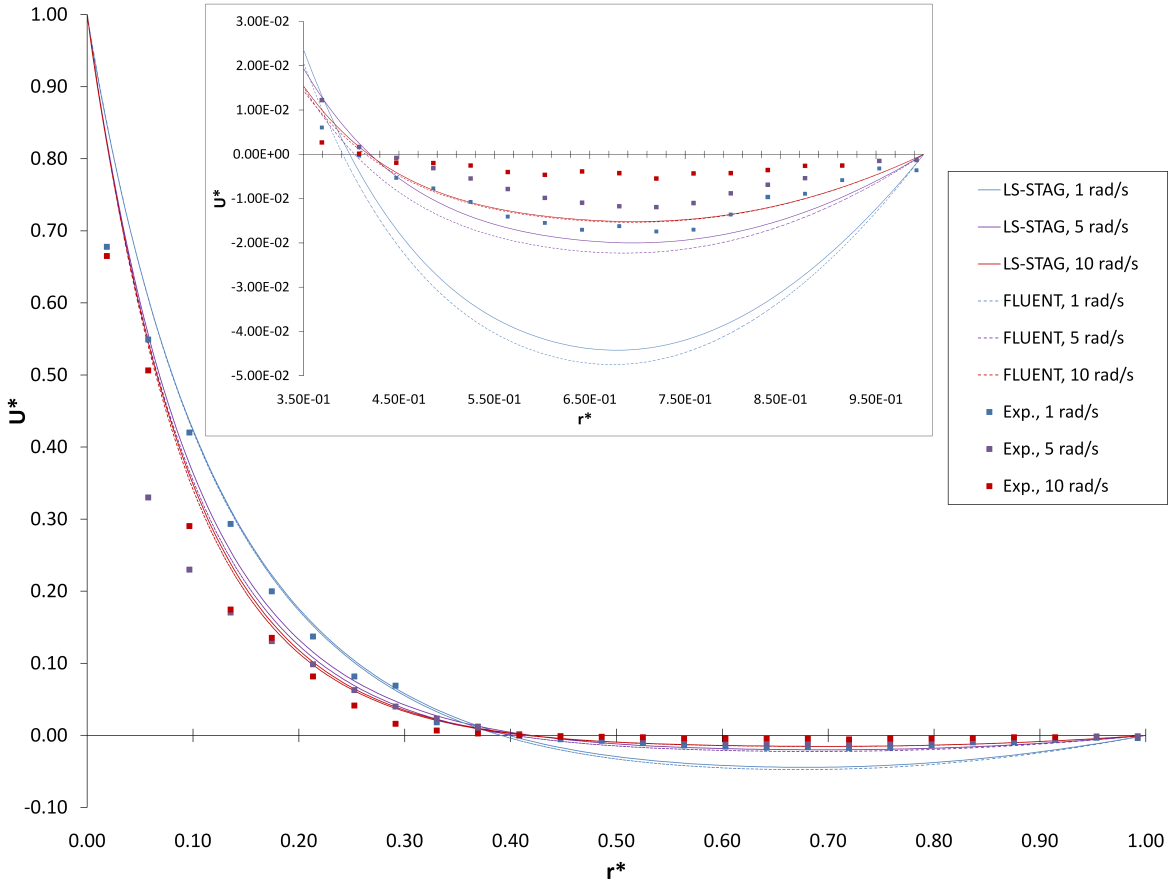


Figure 7: Nondimensional velocity profiles $U^* = v_\theta(r^*, \theta = 0)/r_i\Omega$ with $r^* = r/e_{\max}$ for various angular velocities Ω given by PIV measurement and numerical simulations (xanthan 10%, $\delta = 0.75$).

We now study the structure of the secondary flow for Newtonian and shear-thinning fluids. For evaluating the critical eccentricity, we have performed a series of computations for bracketing the value of δ_c with a ± 0.01 tolerance. In order to understand the onset of the recirculation zone, we have computed for each simulation the moments ratio $R_{i/o} = |M_i/M_o|$ where M_i and M_o are the moment of the viscous forces

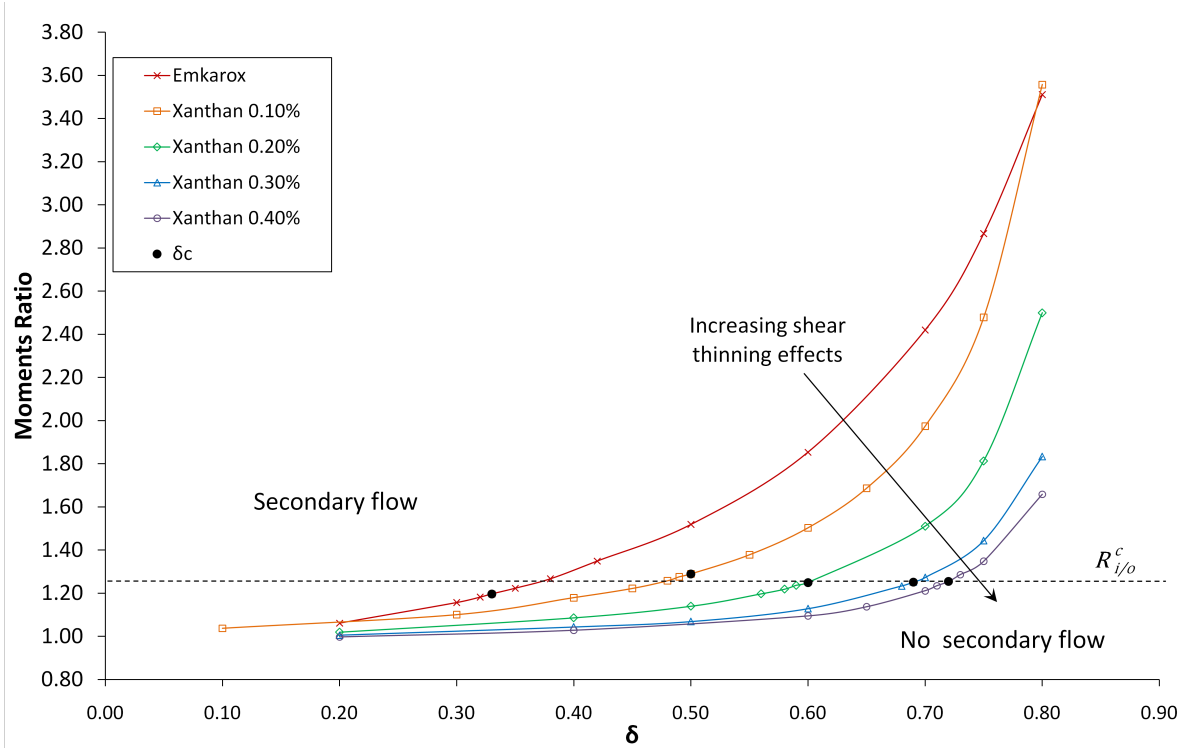


Figure 8: Moments ratio $R_{i/o}$ versus cylinder eccentricity δ for angular velocity $\Omega = 10 \text{ rad} \cdot \text{s}^{-1}$. The critical eccentricity δ_c for the onset of separation is shown for each fluid with black circles.

acting on the inner and outer cylinders respectively. The results obtained for the various fluids for cylinder rotation $\Omega = 10 \text{ rad} \cdot \text{s}^{-1}$ are summarized in Fig. 8. For the Emkarox (Newtonian) fluid, our computations give the value $\delta_c = 0.33 \pm 0.01$ which is in agreement with the value $\delta_c = 0.332424$ obtained analytically in Refs. [11] (note that the FLUENT computations of [6, 5] gives $\delta_c = 0.40 \pm 0.025$). Further computations with Newtonian fluids (not shown here) at various viscosities and cylinder rotations gave similar results, which tend to confirm that the onset of separation has a purely geometrical nature. For non-Newtonian fluids, Fig. 8 shows that the shear-thinning effects clearly delay the apparition of the recirculation zone ; for example, the critical eccentricity is $\delta_c = 0.72 \pm 0.01$ for xanthan 0.40% while FLUENT computations give $\delta_c = 0.70 \pm 0.025$. The most striking results of this figure is that, for both Newtonian and shear-thinning fluids, secondary flow occurs for a momentum ratio greater than the critical value $R_{i/o}^c \simeq 1.2$. It can also be observed that the size of the recirculation zone grows with the value of $R_{i/o}$. Further computations at various cylinder rotations Ω are under way to firmly correlate the moment of the forces at the cylinders with the onset, size and strength of the recirculation zone for non-Newtonian fluids.

Another phenomenon of interest is the position of the secondary flow with respect to the flow parameters. For Newtonian fluids in the creeping regime, the recirculation zone is symmetric and centered on the axis $\theta = 0$. When the Reynolds number is increased, the secondary flow moves downstream due to inertia effects : Ref. [11] showed that the position of the eddy center depends linearly on the inverse of the kinematic viscosity η/ρ . For shear-thinning fluids, the position of the secondary flow is not as easily predictable : for example, we plot on Fig. 9 the streamlines of xanthan flows at increasing concentrations, which correspond to increasing shear-thinning properties. We clearly observe a non-monotonous displacement of the secondary flow with respect to the the shear-thinning property. In particular, for xanthan 0.10% the vortex moves upstream of the flow, and for xanthan 0.40% the shear-thinning and inertia effects compensate to maintain the secondary flow at a centered position. These phenomena, which are absent from Newtonian flows, result from a complex interplay between shear-thinning effects, inertia and flow geometry. Further study is under way to correlate the position of the recirculation zone with a Reynolds number that takes into account the aforementioned flow parameters.

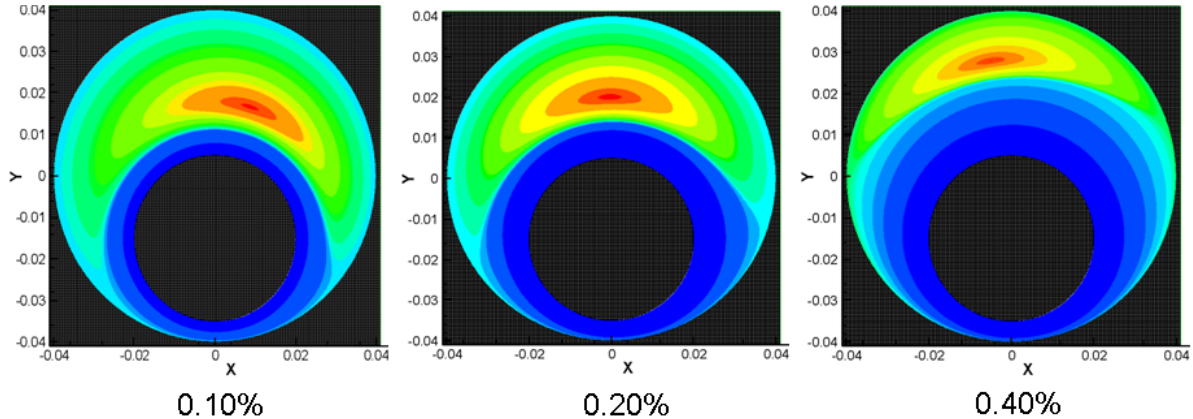


Figure 9: Displacement of the secondary flow for increasing concentrations of xanthan ($\Omega = 20 \text{ rad} \cdot \text{s}^{-1}$, $\delta = 0.75$).

4 Conclusion and Future Work

We have presented in this paper an extension of the LS-STAG immersed boundary method to the computation of non-Newtonian flows. The main numerical difficulty was the computation of the shear rate and non-Newtonian viscosity in the cut-cells near the immersed boundary, where the viscous effects are predominant. This has been achieved with the help of two features developed previously in [2, 4] for Newtonian and viscoelastic flows : the staggering of the components of the rate-of-strain tensor in the cut-cells and the special quadratures developed for the components of the viscoelastic stress tensor.

The accuracy of the non-Newtonian computations has been checked for the Taylor-Couette flow of power-law fluids for which an exact solution exists. The method has been used for computing the secondary flow of shear-thinning fluids between eccentric cylinders, for which experimental and numerical results are available. The next step is now to combine our non-Newtonian and viscoelastic discretization into a realistic constitutive equation of practical interest, which would take into account the shear-thinning and elastic behavior of the liquids.

References

- [1] Y. Cheny and O. Botella. An immersed boundary/level-set method for incompressible viscous flows in complex geometries with good conservation properties. *Europ. J. Comput. Mech.*, **18**, 561-587, 2009.
- [2] Y. Cheny and O. Botella. The LS-STAG method : A new immersed boundary / level-set method for the computation of incompressible viscous flows in complex moving geometries with good conservation properties. *J. Comput. Phys.*, **229**, 1043-1076, 2010.
- [3] O. Botella and Y. Cheny. The LS-STAG method for viscous incompressible flows in irregular geometries: Basics of the discretization and application to viscoelastic flows. In *American Society of Mechanical Engineers, Fluids Engineering Division (Publication) FEDSM*, volume 1, pages 2441-2451, 2010.
- [4] Y. Cheny and O. Botella. *Application of the LS-STAG Immersed Boundary Method to Viscoelastic Flow Computations*. *Computers & Fluids*, in Review.
- [5] C. Rigal. *Comportement de fluides complexes sous écoulement : Approche expérimentale par résonance magnétique nucléaire et techniques optiques et simulations numériques*. PhD Thesis, Institut National Polytechnique de Lorraine, 2012.
- [6] C. Rigal, C. Baravian, G. Belbelkacem, S. Skali-Lami, and M. Lebouché. Shear thinning influence on the secondary flow in eccentric cylinders: a rheo-PIV study. *Exp. Fluids, in revision*.
- [7] F. Gibou, R. P. Fedkiw, Li-Tien Cheng, and M. Kang. A second-order-accurate symmetric discretization of the Poisson equation on irregular domains. *J. Comput. Phys.*, **176**, 205-227, 2002.
- [8] R. W. C. P. Verstappen and A. E. P. Veldman. Symmetry-preserving discretization of turbulent flow. *J. Comput. Phys.*, **187**, 343-368, 2003.

- [9] R. B. Bird, R. C. Armstrong, and O. Hassager. *Dynamics of Polymeric liquids*. Wiley-Interscience, New-York, 1987.
- [10] M.S. Darwish and J.R. Whiteman. Numerical modeling of viscoelastic liquids using a finite-volume method. *J. Non-Newtonian Fluid Mech.*, **45**, 311-337, 1992.
- [11] B. Y. Ballal and R. S. Rivlin. Flow of a Newtonian fluid between eccentric rotating cylinders: Inertial effects. *Archive for Rational Mechanics and Analysis*, **62**:237–294, 1976.
- [12] C. Shu, L. Wang, Y. T. Chew, and N. Zhao. Numerical study of eccentric Couette-Taylor flows and effect of eccentricity on flow patterns. *Theoretical and Computational Fluid Dynamics*, **18**:43–59, 2004.
- [13] S. Jarny and P. Coussot. Caractérisation des écoulements de pâte dans une géométrie Couette. *Rhéologie*, **2**:52–63, 2002.